Geophysical Journal International

Geophys. J. Int. (2024) **236,** 593–606
Advance Access publication 2023 October 25
GJI Seismology

https://doi.org/10.1093/gji/ggad421

Seismic imaging of the Northern Andean subduction zone from teleseismic tomography: a torn and fragmented Nazca slab

E. E. Rodríguez [1,2] S. L. Beck,[1] M. Ruiz,[3] A. Meltzer,[4] D. E. Portner [5,6] S. Hernández,[3] M. Segovia,[3] H. Agurto-Detzel [7] and P. Charvis[8]

[1] *Department of Geosciences, University of Arizona,* 1040 *E.* 4[t8] *St., Tucson, AZ* 85721*, USA. E-mail: eer@lanl.gov*
[2] *Los Alamos National Laboratory, Los Alamos, NM 87545, USA*
[3] *Instituto Geofisico at the Escuela Politécnica Nacional, Av. Ladrón de Guevara E*11-253*, Quito* 170525*, Ecuador*
[4] *Department of Earth and Environmental Sciences, Lehigh University,* 9*A STEPS Bldg.* 1 *W. Packer Ave., Bethlehem, PA* 18015*, USA*
[5] *School of Earth and Space Exploration, Arizona State University, Tempe, AZ* 85281*, USA*
[6] *Department of Earth and Environmental Science, New Mexico Institute of Mining and Technology, Socorro, NM* 87801*, USA*
[7] *Geophysical Institute (GPI), Karlsruhe Institute of Technology,* D-76187 *Karlsruhe, Germany*
[8] *Observatoire de la Côte d'Azur, Université Côte d'Azur, IRD, CNRS, Géoazur, Valbonne 06304, France*

Accepted 2023 October 17. Received 2023 October 16; in original form 2023 June 23

SUMMARY

The Nazca-South America subduction zone in Ecuador is characterized by a complicated along-strike geometry as the slab transitions from flat slab subduction in the south, with the Peruvian flat slab, to what has been characterized as 'normal' dipping subduction beneath central Ecuador. Plate convergence additionally changes south to north as the trench takes on a convex shape. Highly heterogeneous bathymetry at the trench, including the aseismic oceanic Carnegie Ridge (CR), and sparse intermediate-depth seismicity has led many to speculate about the behaviour of the downgoing plate at depth. In this study, we present a finite-frequency teleseismic *P*-wave tomography model of the northern Andes beneath Ecuador and Colombia from 90 to 1200 km depth. Our model builds on prior tomography models in South America by adding relative traveltime residuals recorded at stations in Ecuador. The complete data set is comprised of 114 096 relative traveltime residuals from 1133 stations across South America, with the added data serving to refine the morphology of the Nazca slab in the mantle beneath the northern Andes. Our tomography model shows a Nazca slab with a fragmented along-strike geometry and the first teleseismic images of several proposed slab tears in this region. At the northern edge of the Peruvian flat slab in southern Ecuador, we image a shallow tear at 95–200 km depth that appears to connect mantle flow from beneath the flat slab to the Ecuadorian Arc. Beneath central Ecuador at the latitudes of the CR, the Nazca slab is continuous into the lower mantle. Beneath southern Colombia, the Malpelo Tear breaks the Nazca slab below ∼200 km depth.

Key words: South America; Seismic tomography; Dynamics of lithosphere and mantle; Subduction zone processes.

1 INTRODUCTION

The northern Andean margin in Ecuador and western Colombia is characterized by ongoing subduction of the Nazca plate beneath South America and the presence of accreted oceanic terranes comprising the western margin of the overriding plate. Along the northern Andean margin, the Nazca plate is notably young, ranging from ∼30 to 9 Ma at the trench compared to > 30 Ma south of the Grijalva Fracture Zone (Grijalva FZ, Fig. 1, e.g. Seton *et al.* 2020). The Nazca plate converges with South America at a rate of ∼5.6–6 cm yr^{-1} in the direction of ∼81°–83° N (Trenkamp *et al.* 2002). Convergence is increasingly oblique north of Ecuador following the convex trench. The Nazca plate at these latitudes is characterized by a heterogeneous bathymetry, comprised of various fracture zones and failed rifts related to the reorganization of the Nazca, Cocos, and Farallon plates and the Galápagos hotspot track (e.g. Lonsdale & Klitgord 1978). Among these, the Carnegie Ridge (CR) is an aseismic, oceanic ridge formed at the Galápagos hotspot with ∼19 km thick oceanic crust and 1 km of bathymetry that is presently subducting at the trench between ∼2° S to 0.5° N (e.g. Gailler *et al.* 2007).

Relatively sparse intermediate-depth slab-seismicity beneath Ecuador has made it difficult to discern the upper-mantle geom-

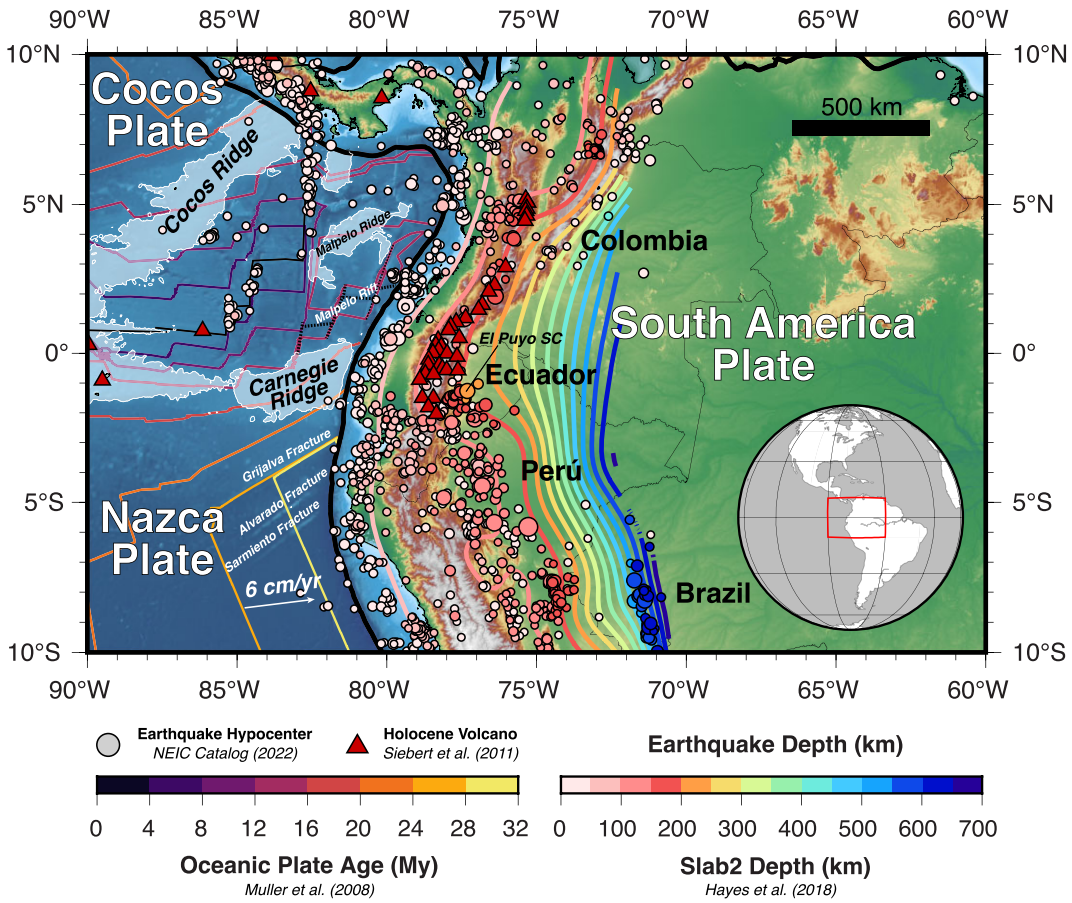

Figure 1. Tectonic map of northwestern South America. Circles denote the location of $M > 5.0$ earthquakes from the NEIC catalogue (1960–2022) and are coloured by depth and scaled by magnitude. Red triangles represent the location of Holocene volcanoes (Siebert *et al.* 2011). Ocean plate ages are contoured on the downgoing plate (Muller *et al.* 2008) and Slab2 contours of the top of the Nazca slab (Hayes *et al.* 2018) are shown with the same colour scale as earthquake depth. Aseismic ridges are shaded in white by their −2300 m bathymetric contour.

etry of the downgoing Nazca plate below 200 km depth (Fig. 1). South of ∼2° S earthquake hypocentres reveal slab dipping at ∼10°–20° at ∼100 km depth for ∼600 km inboard of the trench before re-steepening, marking the northern continuation of the Peruvian flat slab. North of ∼2° S the slab resumes a more normal angle of subduction (∼20°–45°) and an active volcanic arc is present, corresponding to the southern extent of the Northern Andean Volcanic Zone. Beneath the volcanic arc in central Ecuador, intermediate-depth seismicity disappears below 120 km depth, with very few earthquakes recorded within the slab (Fig. 1, Gutscher *et al.* 1999; Guillier *et al.* 2001; Yepes *et al.* 2016; NEIC 2022).

Tectonic models of the region from earthquake hypocentre studies associate this discrete change in seismicity with the inboard projection of the Grijalva FZ (Fig. 1, Gutscher *et al.* 1999; Yepes *et al.* 2016). The Grijalva FZ is an old scarp which places ∼30 Ma crust next to 21 Ma crust across the fracture (e.g. Hardy 1991). Gutscher *et al.* (1999) and Yepes *et al.* (2016) cite the Grijalva FZ as a controlling feature for the anomalous pattern in seismicity. For Gutscher *et al.* (1999), the FZ provides a zone of weakened lithosphere which makes it predisposed to tearing, suggesting the CR has flattened the slab to the north and is torn along the FZ to accommodate differences in slab buoyancy (Gutscher *et al.* 1999). They suggest that northern edge of the CR is additionally torn in a similar fashion along the Malpelo fossil rift (∼2.8 ° N; Fig. 1, Gutscher *et al.* 1999), an old spreading centre which failed ∼8 Ma (e.g. Hardy 1991). The lack of deeper intermediate seismicity in the Gutscher *et al.* (1999) model is due to the flattening of the slab. Rosenbaum *et al.* (2019) similarly infer a slab tear in the same region based on analysis of tension axes from focal mechanisms which exhibit NE-SW extension within the El Puyo seismic cluster (Fig. 1) and the spatial relation of a backarc volcano, Sumaco, which displays geochemical signals associated with an upper-mantle melt source. In this model, the slab is tearing locally along the edge of the Peruvian flat slab and El Puyo seismic cluster (Rosenbaum *et al.* 2019).

In contrast, Yepes *et al.* (2016) point to the difference in age, ∼9 Ma, across the Grijalva FZ to explain the lack of seismicity. In their model, there are no tears along the margin or significant flattening of the slab due to the CR (Yepes *et al.* 2016). Instead, the lack of seismicity in the north is attributed to the younger slab being too warm to produce earthquakes at depth (Yepes *et al.* 2016).

In this study, we present a finite-frequency teleseismic *P*-wave tomography model of the northern Andes beneath Ecuador and Colombia from 90 to 1200 km depth to improve our knowledge of the geometry of the slab and identify tears in the slab. Our model builds on prior tomography models in South America by adding relative traveltime residuals recorded at stations in Ecuador to improve the tomographic images of the Nazca slab beneath Ecuador and Colombia.

1.1 Previous seismic imaging of the Nazca slab beneath Ecuador and Colombia

Tomographic studies of the Nazca slab beneath the northern Andes remain challenging, particularly below ∼150 km depth, due to the limited slab seismicity, and an uneven distribution of publicly available seismic data from eastern Ecuador and western Brazil. Global tomography models reveal two alternate regional images of the Nazca slab in northern South America: (1) a continuous slab along the margin from the top of the subduction zone into the lower mantle (e.g. Montelli *et al.* 2004; Simmons *et al.* 2012) and (2) a discontinuous slab anomaly in the upper mantle, where no slab is present near the latitudes of Ecuador (e.g. Li *et al.* 2008; Mohammadzaheri *et al.* 2021). Recent teleseismic tomography models in this region combined data from across the South America continent to reveal a continuous image of the Nazca slab extending from 100 to 1000 km depth beneath much of South America (Portner *et al.* 2020; Rodriguez *et al.* 2021). Both studies were notably limited in lateral resolution in the upper ∼200 km in beneath Ecuador and southern Colombia due to persistent gaps in station coverage for the northern Andes. Similarly, an adjoint waveform tomography study from Ciardelli *et al.* (2022) imaged a continuous Nazca slab beneath northern South America.

Local tomography studies from Araujo *et al.* (2021), focus on the megathrust interface using crustal seismicity within the region. In their study they image a continuous Nazca slab within the upper ∼120–200 km across northern Ecuador. At ∼2° S near the Puyo seismic nest (Fig. 1), Araujo *et al.* (2021), postulate the presence of a tear in the Nazca slab (above ∼120 km) beneath central Ecuador, but the limited intermediate-depth seismicity in Ecuador limits their model to the upper 150 km for most of the margin.

In this study, we update the SAM5_P_2019 teleseismic *P*-wave velocity model from Portner *et al.* (2020), with particular emphasis on improving our image of the Nazca slab beneath Ecuador and southern Colombia. We enlarge their *P*-wave residual data set by adding more than 30 000 new arrival time picks recorded at 20 new stations, totalling 149 stations, deployed across Ecuador and Colombia. Additionally, we modify the model geometry such that the smallest grid spacing is centred around Ecuador to refine resolution in the study region. Results from this model update illuminate a more complex geometry of the Nazca-South America subduction zone in the northern Andes than previously seen extending from 90 to 1000 km depth.

2 DATA AND METHODS

2.1 Data

We combine relative *P*-wave traveltime residuals from Portner *et al.* (2020; $n = 83\,675$) with 34 518 new relative *P* and *PKiKP* residuals recorded at stations across Ecuador and Colombia from the Ecuador National Seismic Network (RENSIG; Ruiz 2016; Alvarado *et al.* 2018), Red Sismológica Nacional de Colombia (Servicio Geológico Colombiano 1993) and temporary station deployments following the 2016 Pedernales earthquake (Regnier *et al.* 2016; Meltzer *et al.* 2019, Fig. 2). Following Portner *et al.* (2020), we incorporate $> M5.0$ earthquakes from teleseismic distances of 30°–90° for *P* ($n = 30\,432$) and 155°–180° for *PKiKP* ($n = 4086$) arrivals recorded at 141 stations in Ecuador and 8 stations in Colombia (Fig. 2 and Figs S1–S3, Supporting Information). Arrival times are picked in four frequency bands: 0.5–1.5 Hz (26.9 per cent of the full data set), 0.2–0.8 Hz (29.7 per cent), 0.1–0.4 Hz (19.5 per cent) and 0.04–0.16 Hz (23.9 per cent), on the vertical component using the multichannel cross-correlation technique of VanDecar & Crosson (1990), modified by Pavlis & Vernon (2010). Following data exclusion related to duplicate picks and data outliers (e.g. residuals > 1.5 s), our final data set includes 114 096 relative traveltime residuals from 1133 stations across South America and 2340 unique events.

Traveltime residuals are calculated relative to the 1-D IASP91 *P*-wave velocity model (Kennett & Engdahl 1991). Traveltimes are corrected for differences in crustal thickness from the 1-D IASP91 model using the same crustal model from Portner *et al.* (2020) with a revised crustal model for Ecuador from Koch *et al.* (2021; Fig. S2, Supporting Information). We additionally correct station traveltimes to account for the relatively fast forearc observed throughout the Northern Andean margin (e.g. Araujo *et al.* 2021; Lynner *et al.* 2020). Relative residuals of each event are demeaned before inclusion in our inversion (Fig. 3c).

2.2 Tomographic inversion

Our final *P*-wave velocity model was created using the finite-frequency teleseismic tomography inversion method of Schmandt & Humphreys (2010). The model domain extends from 36 to 1450 km depth and is parametrized such that the smallest lateral node spacing is beneath Ecuador, at 35 km in width, and widens laterally to 115 km across most of the continent of South America to preserve the original expanse of the Portner *et al.* (2020) data set (Fig. 3 and Fig. S3, Supporting Information). Model nodes additionally dilate with depth, expanding vertically from 24 to 70 km.

Following Portner *et al.* (2020), rays are initially traced through the model using the 1-D IASP91 *P*-wave velocity model (Kennett & Engdahl 1991) and the sensitivity of each ray within the model is approximated using the first Fresnel zone (Dahlen *et al.* 2000). After an initial inversion using the 1-D velocity model is created we update the travel paths of rays through the resulting 3-D velocity model using the FMTOMO wave-front tracking algorithm from de Kool *et al.* (2006) and Rawlinson *et al.* (2006) and re-invert. This process is repeated iteratively four times, until the resulting model becomes stable (e.g. the data variance no longer improves; Fig. S4, Supporting Information). We additionally choose smoothing and damping parameters of 4 and 5, respectively, based on L2-norm analysis of the model (Fig. S5, Supporting Information). Our choice in model parameters results in a 70 per cent variance reduction of our data. We include comparisons to the SAM5_P_2019 teleseismic *P*-wave velocity model from Portner *et al.* (2020) in Supporting Information, Fig. S6.

2.3 Resolution tests

To understand the resolvability of our model, we rely on a hit-quality measurement, following Schmandt & Humphreys (2010), and a suite of synthetic tests using the event-station geometry of our data set. The hit quality is a parameter used as a proxy to estimate the number of crossing rays within each of our model nodes. It is based on the number of rays in the node and weighted by the number of backazimuthal bins sampled, normalized to 1.0. For example, a 0.2 hit-quality score represents a node which has more than two backazimuth bins sampled, between 11–20 rays within the node or a combination of both. To estimate an appropriate hit-quality threshold for our model, we rely on the synthetic tests described below.

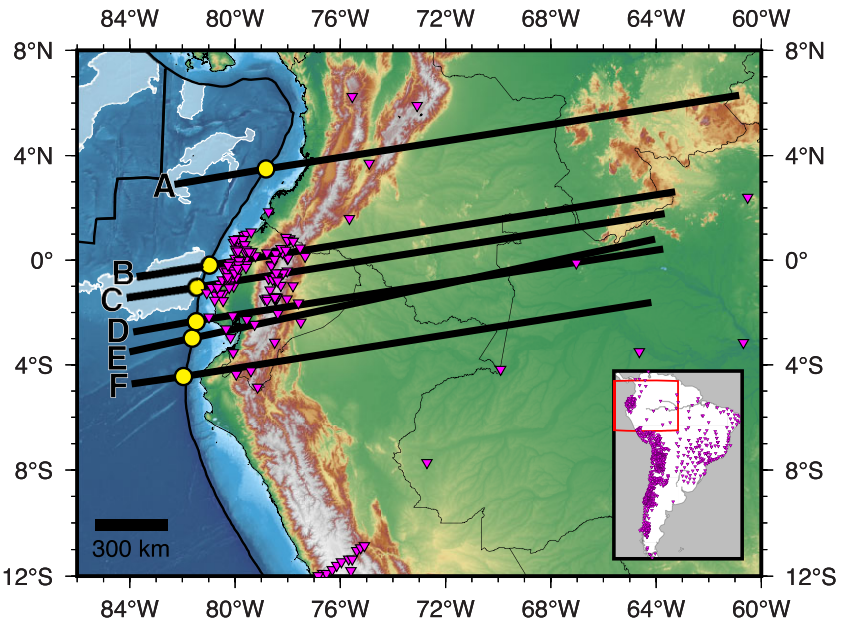

Figure 2. Stations in northwestern South America. Location of stations used in our model represented by magenta inverted triangles. Black lines show the location of cross-sections show in Figs 5 and 7. Yellow circles correspond to the trench location for each cross-section. Inset: all stations used in our inversion. Aseismic ridges are outlined in white by their −2300 m bathymetric contour.

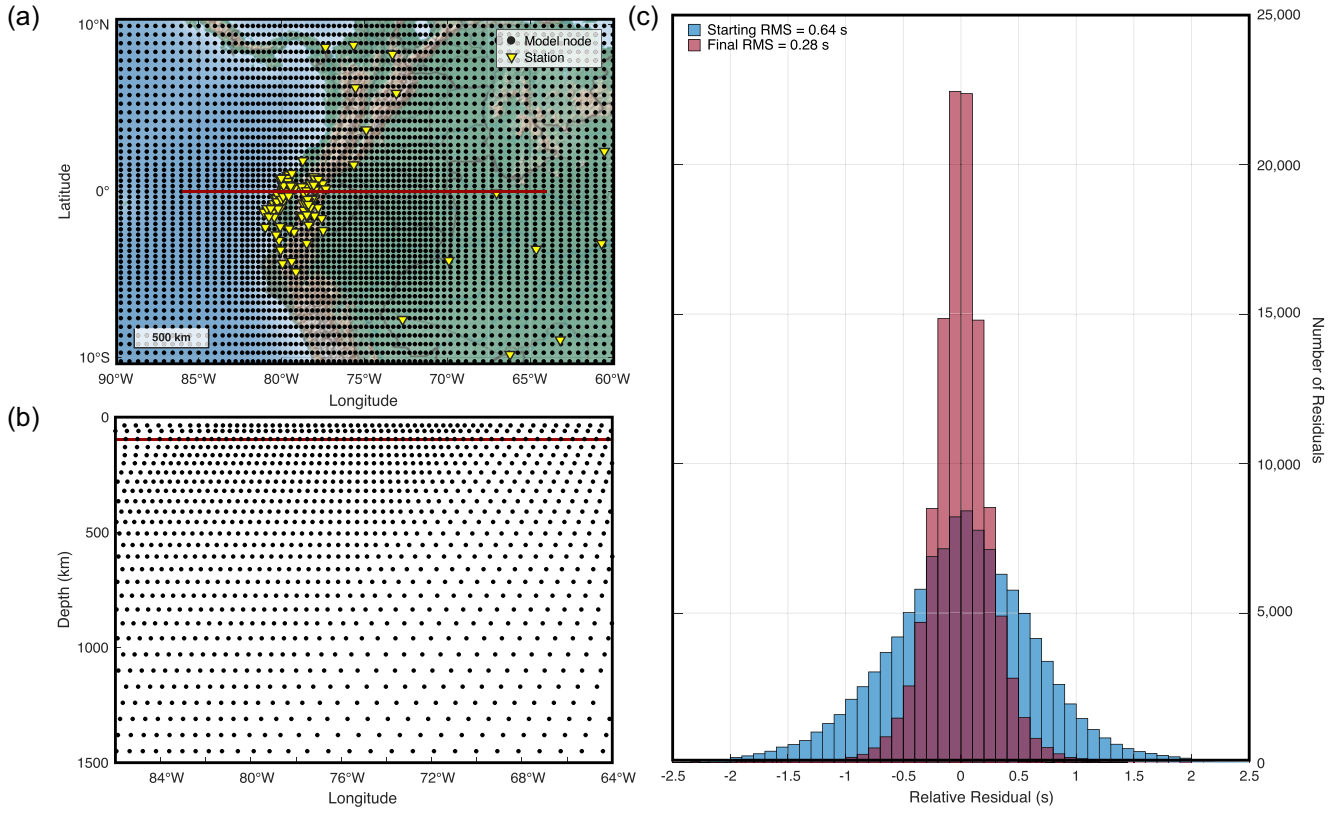

Figure 3. Model information. (a) Map of model node centres (black dots) used in our model at 95 km depth in northwestern South America. Yellow inverted triangles show the location of stations used in our inversion. The red line shows the location of the cross-section shown in subplot B. (b) A cross-section through our model showing model node centres (black circles) at depth. The red line shows the location of the cross-section in (a). (c) The blue histogram shows the distribution of the relative residuals used in our model after crustal and fast-forearc traveltime corrections and demeaning. The red (semi-transparent) histogram shows the distribution of the relative residuals in our final model, after the inversions.

The first synthetic test created is a synthetic checkerboard. In this test, we input alternating anomalies of ± 5 per cent d*Vp* into our model comprising 2 × 2 × 2 model nodes, with 2 nodes of 0 per cent d*Vp* in between (Fig. 4, and Figs S7 and S8, Supporting Information). The results of this test reveal that within the ≥ 0.2 hit-quality contour we recover on average ∼50 per cent of our input anomaly beneath Ecuador between 95 and 1200 km depth. Outside of the ≥ 0.2 hit-quality contour we recover on average < 10 per cent of our synthetic input. The highest amplitudes recovered (>50 per cent of our input anomaly on average) are within the upper 400 km depth beneath Ecuador with very little lateral smearing between nodes (Fig. 4). At shallow (<400 km) depths beneath Colombia, we recover very little of our input anomaly (<20 per cent on average) but do accurately recover the anomaly polarity at the centre of each input checker.

Below 400 km depth the amplitudes of the recovered checkers are diminished, but the input pattern is recovered with very little lateral and vertical smearing between nodes (Fig. 4). Beneath Colombia, recovery improves significantly to ∼50 per cent of our input. Recovered amplitudes are also higher between 800 and 1200 km where we recover ∼50 per cent of the input anomaly (Fig. 4). The highest recovered amplitudes at this depth are beneath western Brazil, Colombia and northern Perú due to spreading ray geometries from Ecuador. We note lateral smearing which increases with depth and is most prevalent along the edges of the ≥ 0.2 hit-quality contour. For all recovered anomalies, the highest recovered amplitudes occur at the centre of our synthetic input.

In addition to the checkerboard tests, we created a synthetic slab as an input (Fig. 5). The synthetic slab was created by tracing the Slab2 contour of the Nazca plate from Hayes *et al.* (2018) into our model. The slab was given a width of three model nodes and an input anomaly of + 5 per cent d*Vp*. We test three potential geometries of the slab: (1) a coherent slab which extends from the surface of our model (36 km) to 935 km depth (Fig. 5, top row; depth slices are included in Fig. S9, Supporting Information), (2) a slab extending from 36 to 935 km depth with a gap from 195 to 580 km depth (Fig. 5, middle row) and (3) a slab which ends at 580 km depth (Fig. 5, bottom row). We additionally include a test which focuses on the model's ability to recover a horizontal tear in the upper 165 km depth beneath south-central Ecuador (Fig. S10, Supporting Information). From the slab recovery tests, we observe the same pattern of recoverability as seen by the checkerboards, with highest resolution at shallow depths beneath Ecuador and deeper depths in the regions surrounding Ecuador.

The highest amplitudes recovered in our synthetic slab occurs beneath central Ecuador between ∼200 and 900 km depth with minimal lateral smearing. In northern Ecuador, where we have the densest ray coverage, we recover the upper 200 km with ∼50 per cent of the input anomaly (Fig. 5, cross-sections b). The synthetic slab gap test shows vertical smearing beneath Ecuador in the mantle transition zone (410–660 km; Fig. 5, middle row); however, the highest recovered amplitudes are at the centre of the input slabs (Fig. 5, middle row), with the exception of the region beneath Colombia, where we recover close to 0 per cent of our synthetic input anomaly in the upper 200 km (Fig. 5, column A). Similarly, our synthetic slab test for a shallow (60–165 km depth) horizontal tear shows there is some vertical smearing however we are largely able to recover the central input anomaly of the slab and tear with minimal lateral smearing (Fig. S10, Supporting Information).

Overall, our synthetic tests reveal that we have best resolution in our model within the upper ∼300 km depth beneath Ecuador and poorest above ∼200 km depth beneath Colombia. At greater depths beneath Ecuador the model recovers less amplitude, while the checkerboard pattern is still recognizable with some lateral smearing along the edges of the ≥ 0.2 hit-quality contour. Recoverability beneath Colombia improves significantly in the lower mantle (>600 km depth). Our synthetic slab tests reveal that for the entire margin of Ecuador and Colombia, we should be able to recover a slab below 200 km depth for Colombia and below a depth of 95 km for Ecuador.

3 RESULTS

Our resulting teleseismic *P*-wave velocity model is shown in selected depth slices and cross-sections in Figs 6 and 7, respectively. Depth slices of the full model are included as Fig. S11 (Supporting Information). Results are shown as per cent d*Vp*, or relative *P*-wave velocities. A prominent feature within our model is a relatively high velocity anomaly which follows the modelled location of the Nazca slab from Slab2 (Hayes *et al.* 2018), where we have resolution, and extends dipping eastward into the lower mantle (Figs 5 and 6). This anomaly overlaps with Wadati–Benioff zone earthquakes where present down to ∼200 km (e.g. NEIC 2022, Figs 6 and 7). We therefore interpret this anomaly as the subducting Nazca plate and will refer to it as the Nazca slab herein.

In the upper 200 km beneath Ecuador, the slab is imaged from ∼2° N to 3° S parallel to the trench with an eastward dip of ∼20° (Fig. 6). From 3° S to ∼5° S, the slab appears to extend farther inboard to ∼500 km from the trench, with a slight dip (∼10°) between 100 and 200 km depth, but shallow resolution at these latitudes is limited by the sparse station distribution (Fig. 6, 90 km depth slice, and Fig. 7f). At the edge of this transition from a flat to more steeply dipping slab, ∼79° W and 3° S, at 95 km depth the slab anomaly is segmented and separated by a series of low velocity anomalies, S1, which extends from beneath the slab to beneath the modern arc (Fig. 7e). This gap in the slab is relatively shallow and laterally limited, extending from only ∼95–165 km depth and ∼100 km across. North of this gap, the slab is relatively continuous beneath the margin of Ecuador.

Below 200 km depth, the slab beneath central Ecuador is continuous to ∼1000 km depth. The angle of the slab is uniform in the upper mantle and begins to flatten in the lower mantle where the slab appears to stagnate at ∼900–1000 km depth (e.g. Figs 7c and d). In south-central Ecuador, we do not recover a slab between 200–600 km depth (Fig. 7f). In southernmost Ecuador, the slab is outside of where we are able to recover predicted slab structure (Hayes *et al.* 2018). However, from 600 to ∼1000 km depth we recover a high velocity anomaly in the lower mantle which connects along strike to the Nazca slab (Fig. 7f). Synthetic slab recovery tests in this area also show we cannot recover the slab in this region between 200–600 km depth (Fig. 5, column F) so we do not interpret the apparent gap in the Nazca slab as reflecting true structure.

Between 0° and 3° N we do not image a coherent high velocity anomaly indicative of the Nazca slab beneath southern Colombia for all depths. Synthetic slab recovery tests of this region show that if a slab anomaly exists in this region, we should be able to recover it below 200 km depth (Figs 7, column A). Below 200 km (Fig. 6), the Nazca slab appears segmented at these latitudes and in some depth slices (320–600 km depth) a low velocity anomaly separates the two segments (S2; Figs 6 and 7).

Our seismic image of the upper mantle in Colombia is limited by station aperture, however, between 4°–8° N a high velocity anomaly is present which follows the Slab2 contour of the Nazca slab and

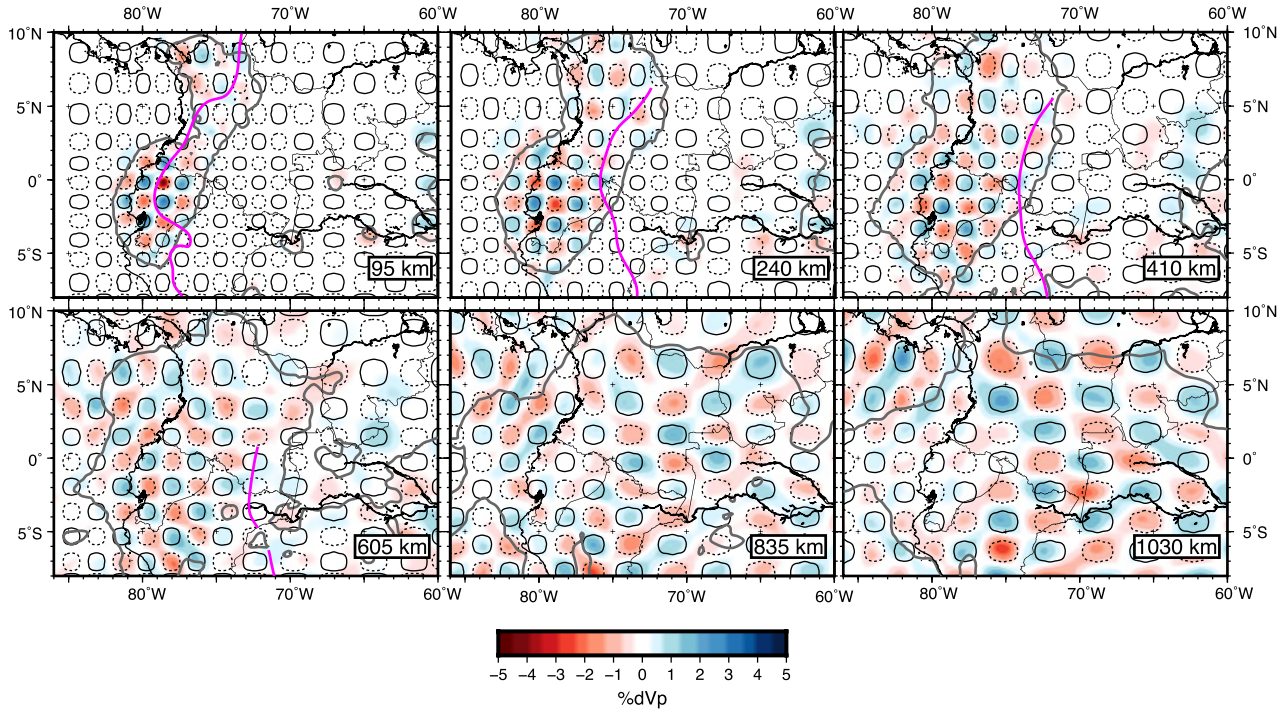

Figure 4. Depth slices through our synthetic checkerboard test. The black solid contours denote the location of + 5 per cent *Vp* as our synthetic input and the dashed contours −5 per cent *Vp*. Each checker is 2 × 2 × 2 model nodes in volume. Depth slices of the synthetic input of the checkerboard test are provided in Fig. S7 (Supporting Information). The grey line shows the ≥ 0.2 hit-quality contour which we use as a marker of resolution in our final model. The magenta line is the top of the Nazca slab from the Slab2 model (Hayes *et al.* 2018) as a point of reference.

Wadati–Benioff zone (Fig. 6). Its connection and continuation in southern Colombia to the slab beneath Ecuador is ambiguous due to an uneven station distribution. This high velocity anomaly extends from 200 to 700 km depth (Fig. 7a). Our resolution tests show we have very poor recovery within the upper 200 km for synthetic slab anomaly in this region and earthquake hypocentres continue where the model does not resolve a slab-like anomaly. The apparent lack of slab in the upper 200 km is therefore not resolvable at these latitudes within the model.

4 DISCUSSION

4.1 Slab tearing beneath Colombia and Northern Ecuador

Our results reveal an image of a fragmented Nazca slab beneath Ecuador and Colombia. North of 4° N, beneath central Colombia we image the slab extending ∼200 km depth into the lower mantle where it appears to terminate at ∼800–1000 km depth (Fig. 7a). Further south, between ∼3° N and 0° we image a gap in the Nazca slab anomaly (Fig. 7b). Earthquake hypocentres in this region extend to ∼150 km depth and the presence of an active arc also suggests that the slab most likely subducts to at least ∼100–150 km depth where arc flux melting is typically initiated (e.g. Syracuse & Abers 2006). The gap in the slab extends to the northern edge of the subducted CR (Fig. 7, cross-section b). Hence, it is a slab gap of over 300 km along strike starting at ∼200 km depth (Fig. 6). In synthetic slab tests (Fig. 5), we recover almost none of the input anomaly above 200 km in this region and therefore suggest that an absence of a slab anomaly above these depths does not imply the absence of a slab. However, at depths deeper than 200 km, a slab is sufficiently recoverable such that its absence in our tomography model is robust evidence for a deeper slab gap.

Sun *et al.* (2022), using teleseismic tomography, image two discrete slabs beneath Colombia. The first is the Caribbean slab which extends north of 5.5° N and overlaps with the second slab which extends southward and is interpreted as the Nazca slab (Sun *et al.* 2022). South of 3° N, their Nazca slab anomaly disappears below ∼230 km depth, consistent with our image of the region (Sun *et al.* 2020; their figs 3 and 5e).

A slab gap in this region has been inferred from several studies including shear wave splitting which shows a change in regional splitting patterns from trench parallel in the north to a more spurious pattern south of 3° N (Fig. 6; Idárraga-García *et al.* 2016), geochemical studies of the arc related to an increase in alkaline volcanism interpreted to be related to an asthenospheric window (Borrero & Castillo 2006), and earthquake hypocentre studies which note a clear decrease in intermediate-depth earthquakes in this region, with sparse seismicity >150 km (e.g. Syracuse *et al.* 2016), compared to north of 3° N. These studies name this gap the Malpelo Tear, with inferred origins related to the subduction of an ancient spreading ridge, the Malpelo Rift (Fig. 1), which presently resides in the trench at 2.8° N (Gutscher *et al.* 1999; Borrero & Castillo 2006; Idárraga-García *et al.* 2016).

4.2 Central Ecuador and the Carnegie Ridge

Beneath central-northern Ecuador, ∼1° S–2° S, where the centre of the CR (Fig. 7, cross-section c) currently enters the trench, we image a continuous Nazca slab extending from 95 to ∼1000 km depth. The slab retains a relatively uniform dip of ∼20° within the

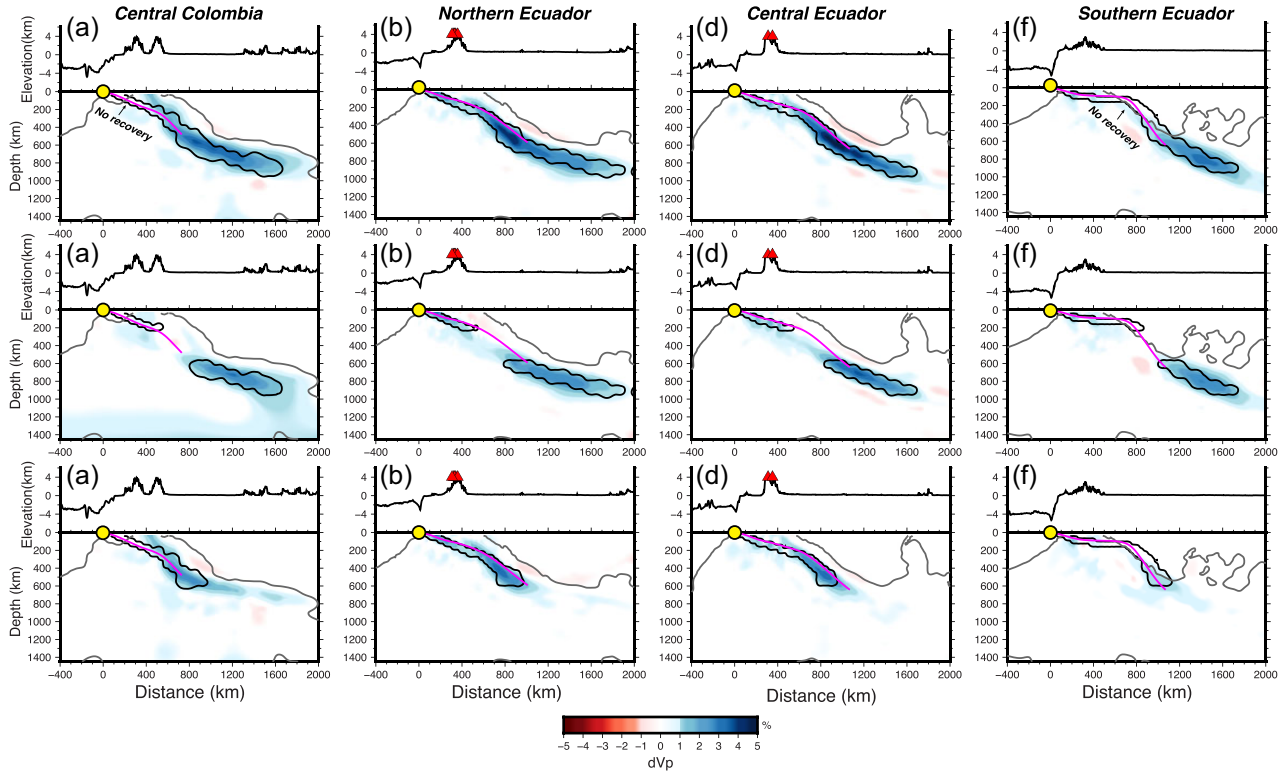

Figure 5. Synthetic slab test cross-sections. Each column shows the same cross-section corresponding to Fig. 2. Each row shows a different slab geometry test. Top row: the synthetic slab extends from 36 to 935 km depth. Additional depth slices are included in Fig. S9 (Supporting Information). Middle Row: the synthetic slab extends from 36 to 935 km depth with a gap from 195 to 580 km depth. Bottom row: the synthetic slab anomaly ends at 580 km depth. For all figures, the black line corresponds to the location of a + 5 per cent *Vp* synthetic input anomaly. The colour map shows the resulting output anomaly. The grey line contours the ≥ 0.2 hit quality.

upper mantle. Despite prior inferences associating the CR to other subducting hotspot tracks along the western South American margin (e.g. Gutscher *et al.* 1999), we see no evidence for local flattening of the slab due to CR subduction. Local earthquake studies have similarly observed no significant changes in the Nazca slab's dip related to the CR (Fig. 7, cross-sections b and c, Guillier *et al.* 2001; Yepes *et al.* 2016; Araujo *et al.* 2021).

The CR is an oceanic ridge, ∼200 km wide, with 1 km of bathymetric relief that formed at the Galápagos hotspot and has an oceanic crustal thickness of ∼19 km as it enters the trench (Sallarès & Charvis 2003; Graindorge *et al.* 2004; Gailler *et al.* 2007). In contrast to along-margin examples of ridge subduction (Nazca Ridge in Peru, Juan Fernandez Ridge in Chile), there does not appear to be a flat slab associated with the thick, buoyant oceanic crust of the CR. Models of the timing of the CR's arrival into the trench vary extensively from 1.4 to 15 Ma (e.g. Gutscher *et al.* 1999; Lonsdale, 2005; Michaud *et al.* 2009; Spikings *et al.* 2010) due to uncertainty in the timing of when the Cocos spreading ridge first reached its current position atop the Galápagos hotspot. Using the current convergence rate of the South America and Nazca plates of 6 cm yr^{-1} as a conservative minimum (Trenkamp *et al.* 2002), this would predict the CR to be anywhere from ∼85 to 900 km in the subduction zone.

There are two scenarios which may in part explain the lack of a flat slab observation: (1) the CR has not subducted as far in the subduction zone as suggested by some models and hence, has not had time to flatten the subducting slab (e.g. Gutscher *et al.* 1999) or to reach a depth of neutral buoyancy; or (2) the above average thickness crust (∼19 km) of the CR does not provide enough buoyancy on its own to flatten the slab even if it has subducted deep into the subduction system. The thick CR oceanic crust off-shore today (Graindorge *et al.* 2004; Gailler *et al.* 2007) suggests that it should have significant buoyancy compared to the surrounding mantle until the thick oceanic crust transforms to eclogite (Fig. S12, Supporting Information; Huangfu *et al.* 2016). Numerous models have suggested additional mechanisms may be required to flatten slabs such as overthrusting of the overriding plate and young age of the subducting lithosphere (van Hunen *et al.* 2002; Huangfu *et al.* 2016), subslab overpressure (Schepers *et al.* 2017), slab-suction (Manea *et al.* 2012), or if additional buoyancy from the sub-slab mantle (Bishop *et al.* 2017). Hence, we cannot be sure if the CR has not subducted far enough into the system to cause flat subduction (except for the very shallow part of the system) or if additional factors are needed. Factors favouring flat subduction in this region are the thick oceanic crust and the young age of the oceanic crust (15–24 Ma) subducting at the trench (Fig. S10, Supporting Information). Factors that do not favour flat subduction are motion of the overriding plate which is part of the Andean block that is moving northward and not overriding the Nazca plate and the warm subduction zone suggesting a shallower depth for the basalt to eclogite transition (∼60–70 km depth; Wada & Wang 2009). Considering that similar factors are considered sufficient to induce slab flattening elsewhere in South America (Peruvian flat slab, Chilean flat slab) when given enough time, we infer it most likely that the CR has not subducted very far into the subduction system.

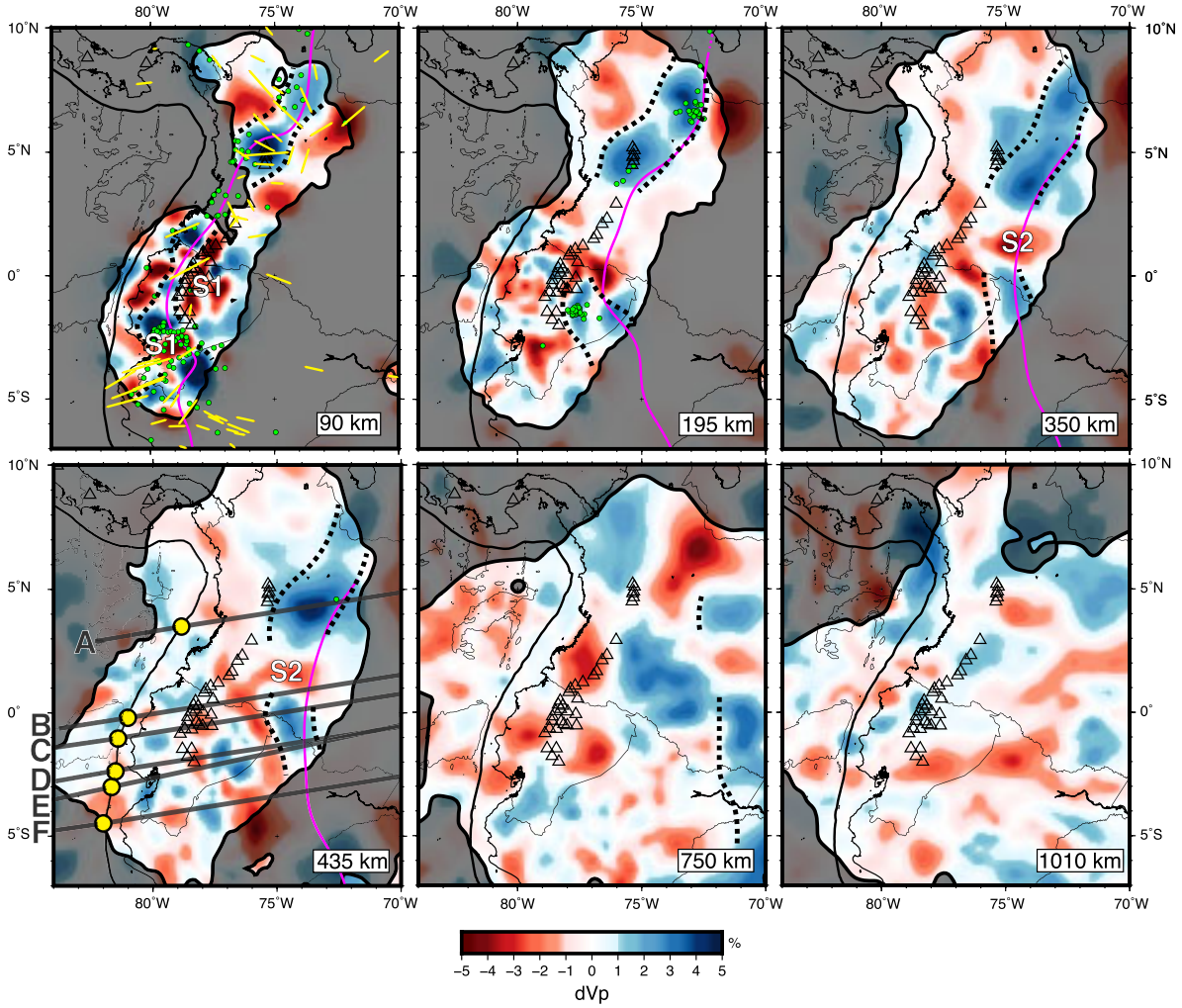

Figure 6. Depth slices through our *P*-wave velocity model. The depth of each map view is denoted in the bottom right corner. Yellow arrows in the top left panel (90 km depth) show the fast-splitting directions of *XKS* waves from Condori *et al.* (2021) and Idárraga-García (2016). Black triangles show the surface location of Holocene volcanoes (Siebert *et al.* 2011). The magenta line represents the top of the Nazca slab at each depth slice from Slab2 (Hayes *et al.* 2018). The thick, solid black line denotes the location of the trench. Green circles correspond to hypocentre locations of $> M4$ earthquakes within 10 km of the depth slice (NEIC 2022). Black dashed lines indicate our interpretation of the subducting slab based on tomography and earthquakes. There are few earthquakes in the slab below ∼200 km. We grey out regions of the model which are below the 0.2 hit-quality threshold. The location of cross-sections shown in Figs 5 and 7 are shown in the bottom left panel (435 km depth). We note that the cross-sections extend outside of the panel (see Fig. 2).

Within the lower mantle, the slab appears to stagnate at ∼1000 km depth beneath central Brazil (Fig. 7; cross-sections c and d). This image of the lower mantle slab is consistent with studies of the slab from Portner *et al.* (2020), whose data are included in this study, Rodríguez *et al.* (2021) and Ciardelli *et al.* (2022). Stagnation of the slab at lower mantle depths (∼1000 km) in our study and other studies are related to possible changes in the rheology of the slab or the viscosity of the surrounding mantle (Portner *et al.* 2020; Rodríguez *et al.* 2021; Ciardelli *et al.* 2022). However, in a model by Faccenna *et al.* (2017), stagnation of the Nazca slab occurs without changes to the properties of the slab or mantle and is invoked simply by the observed westward retreat of the trench which is estimated to be ∼1000 km (Schepers *et al.* 2017).

4.3 Southern Ecuador

In southern Ecuador, above 200 km depth, we observe a small gap in the observed slab anomaly east of the Gulf of Guayaquil, along the northern edge of the Peruvian flat slab (Figs 6 and 7e; anomaly S1). This slab gap extends for ∼100 km in depth, from the top of our resolvable model space, 95 to 200 km depth. We note that we are not able to resolve the top of the tear. The existence of earthquakes within or on the edge of the gap additionally points to the gap being shallower than resolved in our model and is supported by the vertical smearing resolved in our synthetic slab test (Fig. S10, Supporting Information). This slab gap shows a low velocity anomaly (S1), which laterally extends from the southern edge of our model northeastward through the slab gap where it appears to connect with a low velocity anomaly beneath the modern volcanic arc. We interpret this gap to be a localized tear within the Nazca slab. This slab tear is not orientated in the dip direction of the slab; hence its geometry is complex. Below ∼200 km depth the slab looks more continuous.

Similar tears along the South America margin have been predicted and observed at the edges of flat slabs (Antonijevic *et al.* 2015; Hu & Liu 2016; Portner *et al.* 2017) and at the Ecuadorian

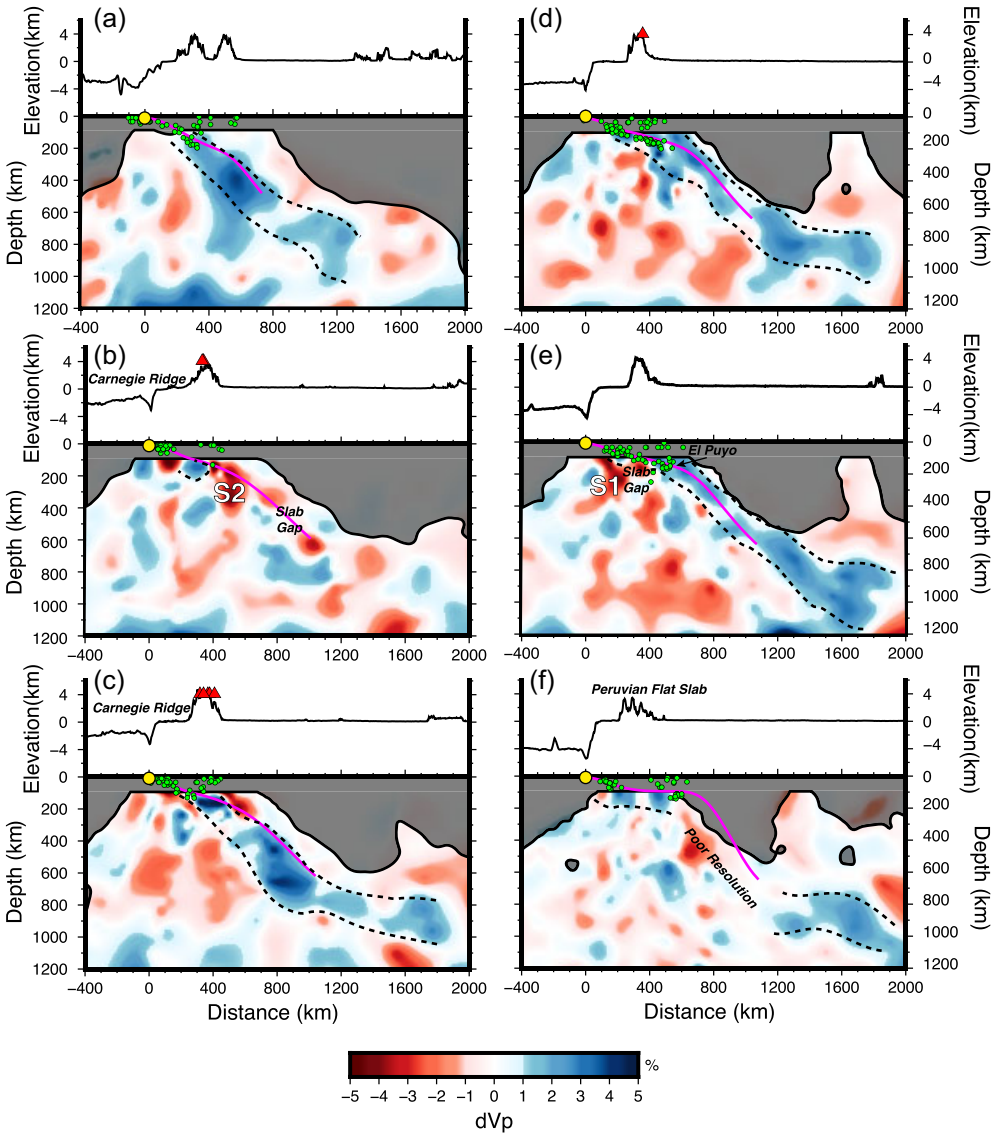

Figure 7. Cross-sections through our *P*-wave velocity model. Plotted above is topography along the cross-section. Red triangles represent the location of volcanoes within 20 km of the cross-section line. The yellow circles correspond to the location of the trench at each cross-section. Green circles represented hypocentres of earthquakes $> M4$ from the NEIC catalogue (NEIC 2022). Black dashed lines indicate our interpretation of the subducting slab based on tomography and earthquakes. We grey out regions of the model which are below the 0.2 hit-quality threshold.

margin (Gutscher et al 1999; Rosenbaum *et al.* 2019). Araujo *et al.* (2021) imaged a tear in their local tomography model at the same location and depth as the previous studies. Araujo *et al.* (2016) interpret this tear as a result of the sharp curvature of the trench and slab in which they describe compressional stresses that buckle the slab at its axis, which is collocated with the El Puyo seismic cluster (Fig. 1; Araujo *et al.* 2021). Alternatively, a slab tear was inferred in the same location by Rosenbaum *et al.* (2019) and Gutscher *et al.* (1999) using the ISC-EHB earthquake catalogue. They inferred a tear based on an abrupt change in seismicity north of the El Puyo seismic cluster (e.g. sparse intermediate seismicity >90 km). Both models propose tearing from extensional forces within the Nazca plate, however they point to different sources: Rosenbaum *et al.* (2019) observed extension within the plate at its transition from flat to normal subduction along the northern edge of the Peruvian flat slab while Gutscher *et al.* (1999) point to tearing of the slab along the Grijalva FZ as a result in the differences in buoyancy caused by a proposed flat slab associated with the CR. The subduction of a fracture zone would additionally introduce more fluids into the oceanic lithosphere, presumably weakening the slab locally (e.g. Ranero *et al.* 2003).

The coincidence of this slab tear along the northern edge of the Peruvian flat slab and the inboard projection of the Grijalva FZ, as well as over the Puyo seismic cluster, which is characterized by downdip, NE-SW oriented extensional focal mechanisms (e.g. Yepes *et al.* 2016; Rosenbaum *et al.* 2019; Vaca *et al.* 2019) leads us to favour a tear by extension. The apparent low velocity anomaly, S1, through the tear and its apparent connection to the volcanic arc suggests flow through this tear between < 95–200 km depth connecting the hot sub-slab mantle beneath the Peruvian flat slab to the mantle beneath the Ecuador arc. Flow through the slab tear is supported by a distinct northward rotation in shear wave splitting directions from trench subparallel to nearly perpendicular between 3°–6° S (Fig. 6; Condori *et al.* 2021). It is possible that the sharp

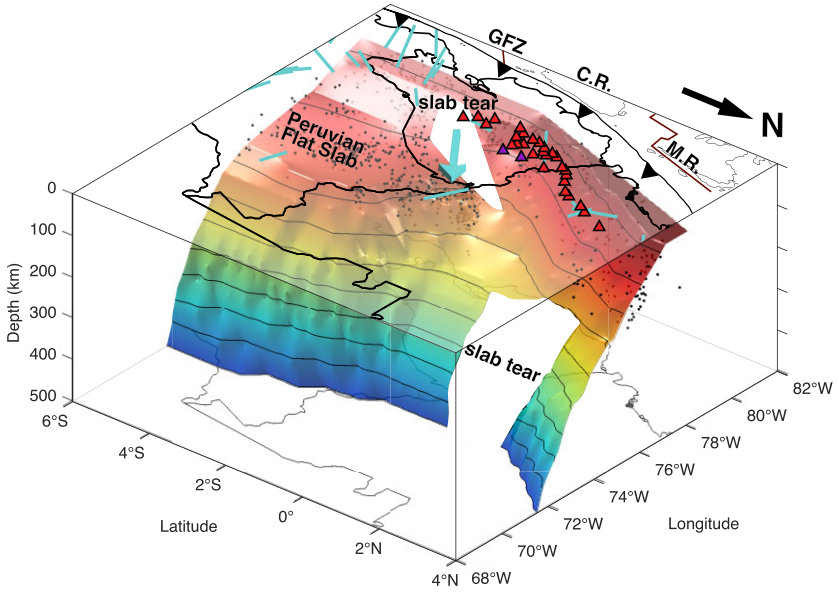

Figure 8. Summary diagram showing the interpretation of our *P*-wave tomography model including the two tears in the slab. The top of the Nazca slab based on our tomographic images is shown as the coloured surface. Black contours are depth of the subducting Nazca plate every 50 km. Black circles show earthquake hypocentres from the NEIC catalogue (NEIC 2022). Red triangles denote the locations of Holocene volcanoes (Siebert *et al.* 2011). Backarc volcanoes, Reventador and Sumaco, are shown in dark purple. Light blue lines show the fast-splitting directions of *XKS* waves from Condori *et al.* (2021) and Idárraga-García (2016). The light blue arrow shows our interpretation of mantle flow through the shallow slab tear. GFZ—Grijalva Fracture Zone; CR—Carnegie Ridge and MR—Malpelo Rift.

transition in the geometry of the subducting slab, both laterally, from flat to steeper, and along-strike coupled with the difference in buoyancy related to the Peruvian flat slab, produced a tear along the edge. The change in mantle flow here and the connection of low velocity anomalies beneath the Nazca slab to the mantle wedge may indicate southwest–northeast flow through the tear (Fig. 8).

Rosenbaum *et al.* (2019) point out that the volcanic arc in Ecuador is broadest in this region, with anomalous backarc volcanism despite the system being in compression (e.g. no backarc extension). Rosenbaum *et al.* (2019) and Ancellin *et al.* (2017) additionally connect changes in the geochemical composition of backarc lavas, most notably at Sumaco volcano, to a proposed tear which exhibits higher alkalinity and rare-earth element enrichment and lower silica content than the rest of the Ecuadorian arc (Rosenbaum *et al.* 2019; Ancellin *et al.* 2017). Other authors have noted a more regional change in the across-arc geochemistry from Sr—Nd-Pb isotopes, inferring a general increase in mantle-derived magmas eastward (e.g. Hidalgo *et al.* 2012; Ancellin *et al.* 2017). Hidalgo *et al.* (2012 and references therein) have noted this change in composition, however the origin of this change and the adakitic signature of the arc in Ecuador is heavily debated with hypotheses including the presence of a slab tear, underplating, changes in sediments in the subduction zone, changes in basement composition and changes in crustal thickness. We note that the geochemical changes across and along the arc are consistent with a slab tear interpretation, however, we acknowledge that adakites can also be generated by assimilation and garnet fractionation in thick Andean crust (Kay *et al.* 2005).

4.4 Slab tearing along the Andean margin

Seismic imaging of the Nazca slab beneath South America reveals the existence of several tears along the margin in addition to those imaged in this study (Fig. 9). These tears have been linked to two main mechanisms which promote internal tearing, both of which are related to the subduction of prominent bathymetric features on the incoming plate. The first is that internal differences in slab buoyancy cause differential rates of slab sinking which must be accommodated by stretching and thinning of the slab and eventual tearing (e.g. Gutscher et al 2000; Hu & Liu 2016). Such tears have been interpreted around both the Peruvian (e.g. this study; Antonijevic *et al.* 2015; Scire *et al.* 2016) and Pampean flat slabs (e.g. Portner *et al.* 2017; Gao *et al.* 2021; Liu & Gao 2022) due to the relative buoyancy differences between the flat slabs and the surrounding lithosphere. In both regions, tears are imaged at the edges of and along the inboard projection of the subducting buoyant Nazca and Juan Fernández Ridges, respectively, which are broadly considered to contribute to the local slab shallowing (Fig. 9, Antonijevic *et al.* 2015; Scire *et al.* 2016; Portner *et al.* 2017; Gao *et al.* 2021; Liu & Gao 2022).

The second mechanism is related to the subduction of lithospheric-scale boundaries or zones of weakness. Such tearing has been inferred in South America associated with differential motion across fracture zones and with window formation at subducting rift zones. These include the Maule tear in Chile associated with the Mocha fracture zone (Pesicek *et al.* 2012), the Malpelo Tear in southern Colombia associated with and the Malpelo Rift in southern Colombia (this study; Borrero & Castillo 2006; Idárraga-García et al 2016) and the Caldas tear in central Colombia associated with the Sandra Rift (Vargas & Mann 2013; Sun *et al.* 2022), though the latter has alternatively been associated with flat slab subduction (Wagner *et al.* 2017) or the northern edge of the Nazca plate (e.g. Cortés & Angelier 2005; Vargas & Mann 2013; Syracuse *et al.* 2016; Sun *et al.* 2022).

The slab tears we image beneath Ecuador and southern Colombia exhibit each of these two primary mechanisms of slab tearing, respectively, and add to this growing body of evidence that the Nazca

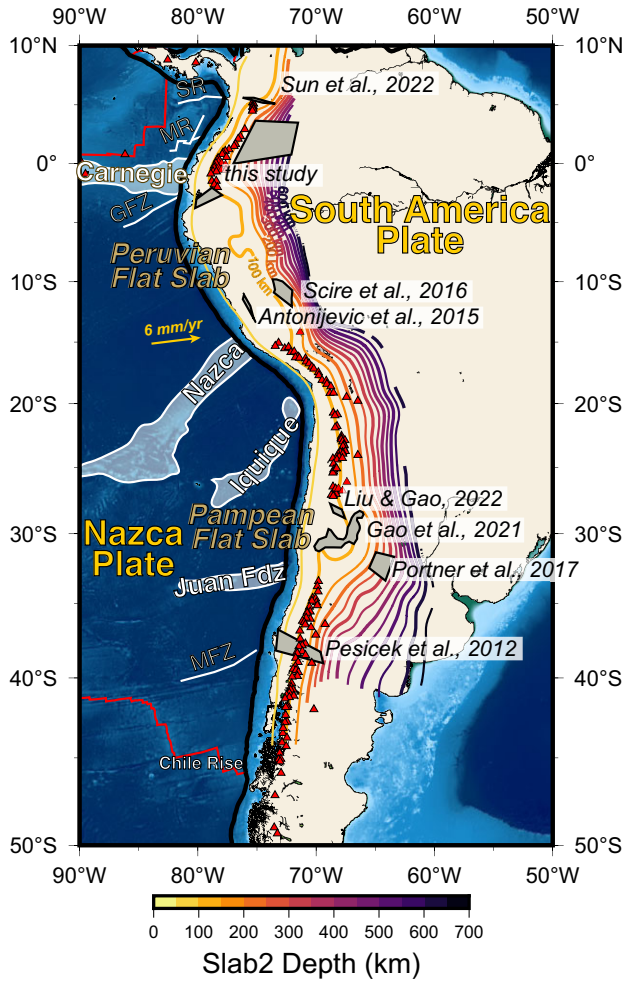

Figure 9. Proposed slab tears along the Andean margin from local and regional tomography studies. Grey polygons show the generalized location of slab tears within the Nazca slab (Antonijevic *et al.* 2015; Scire *et al.* 2016; Sun *et al.* 2022; Liu & Gao 2022; Pesicek *et al.* 2012; Portner *et al.* 2017; Gao *et al.* 2021). Upper-mantle geometry of the top of the Nazca slab is shown as coloured contours at every 50 km depth (see colour scale within, Hayes *et al.* 2018). The thick, solid black line denotes the location of the trench. Red triangles show the locations of Holocene volcanoes (Siebert et al., 2012). Prominent bathymetric features are highlighted in white including the Carnegie, Nazca, Iquique and Juan Fernández (Juan Fdz) aseismic oceanic ridges and major fractures/rifts: SR—Sandra Rift, MR—Malpelo Rift, GFZ—Grijalva fracture zone and MFZ—Mocha Fracture Zone.

slab is torn and deformed, and that heterogeneity in the subducting plate is a controlling factor in Nazca slab fragmentation. A partially fragmented Nazca slab, as opposed to a coherent slab, has significant implications for regional mantle flow and wedge dynamics (Antonijevic *et al.* 2016; Idárraga-García *et al.* 2016; Lynner *et al.* 2017; Schepers *et al.* 2017; Király *et al.* 2020), the evolution of flat slabs (e.g. Antonijevic *et al.* 2015; Taramón *et al.* 2015) and magmatism in the South American cordillera (e.g. Hu & Liu 2016; Gianni *et al.* 2019). Evidence for tears in the Nazca slab along parts of the subduction margin (Fig. 9) call into question the traditional concept of slabs as strong, coherent bodies that passively sink through the upper mantle. Instead, at least parts of the Nazca slab are prone to internal deformation starting as soon as they subduct into the upper mantle.

5 CONCLUSIONS

We present a finite-frequency teleseismic *P*-wave tomography model of the northern Andes beneath Ecuador and Colombia from 90–1200 km depth. Our model builds on the work of Portner *et al.* (2020) to refine the morphology of the Nazca slab in the mantle beneath the northern Andes. Our results show a Nazca slab with a complicated along-strike geometry and the first teleseismic images of several proposed tears in this region. Beneath Ecuador, we image a shallow tear in the upper 200 km along the transition from flat slab subduction beneath Perú to a steeper subducting slab in the north. We infer the origins of this tear to be related to the stretching of the slab locally as it steepens. Additionally, we image a low velocity anomaly which extends through the tear and connects to a low velocity anomaly beneath the modern arc of Ecuador. Flow through this slab tear into the arc could explain the anomalous broadening of the arc and is supported by regional changes of the arc geochemistry.

Inboard of the CR, the Nazca slab is continuous from 90 to 1000 km depth. The slab retains an average dip, ∼20°, into the mantle transition zone where the slab begins to shallow and stagnate at ∼1000 km depth. Our model shows no evidence of the CR flattening the slab below 95 km depth as suggested by some models.

At the border of Colombia and Ecuador, there is no imaged slab anomaly. We do not have resolution above 200 km depth, however, the lack of a slab anomaly below 200 km suggests a resolvable slab tear. This tear, previously named the Malpelo Tear, likely originates from the subduction of the Malpelo fossil rift which is currently at the trench. This tear is relatively small laterally, ∼3° N–0°, but it extends in the lower mantle. North of 3° N we image the northern continuation of the Nazca slab from the top of our resolution at 200 down to ∼800 km depth.

ACKNOWLEDGMENTS

This work was supported by NSF grants EAR-1723065 and EAR-1951202. Thanks to the research and technical staff at Instituto Geofisico at the Escuela Politécnica Nacional (IG-EPN) in Quito Ecuador for excellent logistics and field support. Thanks to the Earthscope PASSCAL Instrument facility for supporting instrumentation used in the U.S. portion of the Pedernales aftershock deployment. Additional instrumentation and data collection came from the Institut de recherche pour le développement (IRD) Géoazur in Nice France, and University of Liverpool, UK. The tomography model from this study will be made available online through the IRIS Earth Model Collaboration with the label SAM6_P_2023_Ecuador.

DATA AVAILABILITY

The data are from the Ecuador National Seismic Network (RENSIG; Ruiz 2016; Alvarado *et al.* 2018), Red Sismológica Nacional de Colombia (Servicio Geológico Colombiano 1993) with open stations provided at the EarthScope Data Center and additional data provided by RENSIG. Data from the temporary station deployments following the 2016 Pedernales earthquake are available at the Earthscope Data Center.

SUPPORTING INFORMATION

Supplementary data are available at *GJI* online.

Figure S1. Data used in our inversion. (a) Map of all event locations used in this study. Circles represent hypocentre locations

colour coded by phase (see the legend) and all are at teleseismic distances for some stations in our entire study. We note that only the station-side path is used in our study, we do not resolve source-side structure. (b) Distribution of event backazimuths coloured by phase (red—direct *P* and blue—*PKiKP*). (c) Histogram of relative residuals used in our inversion coloured by phase. (d) Distribrution of event backazimuths coloured by station locations (purple—full data set and orange—events recorded at stations in Ecuador and Colombia. (e) histogram of relative residuals used in our inversion coloured by station location.

Figure S2. Crustal thickness traveltime correction maps and plots. (a) Each circle shows the location of a station used in the inversion colour coded by the estimated Moho depth used to correct traveltimes. (b) Traveltime corrections for each station (not including a fast forearc correction). (c) Average station traveltime residual for each station before crustal traveltime correction. (d) Average station traveltime residual for each station after crustal traveltime correction. (e) Histogram of traveltime residuals before traveltime correction. (f) Histogram of traveltime residuals after traveltime correction. Traveltime residuals generally improve except for a small cluster at ∼1.6° S where there are red circles indicating that at those stations the crustal traveltime correction adds scatter.

Figure S3. Map of model node centres (black dots) used in our model at 95 km depth in our full model. Yellow inverted triangles show the location of stations used in our final model.

Figure S4. Variance reduction difference vs. number of inversion iterations. This plot summarizes the variance reduction between each 3-D ray tracing iteration. We highlight with a yellow star the iteration used as our final model. Following iteration 4, variance reduction was greatly reduced.

Figure S5. Trade-off analysis curve. Data variance reduction versus L2 model norm for choices of smoothing and damping parameters ranging from 1 to 10 are plotted by the red and blue circles. The solid/dashed lines correspond to constant damping (denoted as D 1–10) and smoothing (denoted as S 1–10) trends, respectively. The model with a damping parameter of 4 and smoothing parameter of 4 (yellow star) were chosen for our final model using the initial 1-D ray tracing.

Figure S6. Comparison cross-sections of our *P*-wave tomography model and SAM5_P_2019 (Portner *et al.* 2020). The left-hand column shows cross-sections through our model and the right through SAM5_P_2019. The location of each cross-section is shown in the map view.

Figure S7. All depth slices through our synthetic checkerboard test. The black solid contours denote the location of + 5 per cent and the dashed contours −5 per cent *Vp* of our synthetic input respectively. Each checker box is 2 × 2 × 2 model nodes in volume. The grey line shows the ≥ 0.2 hit-quality contour which we use as an indication of resolution in our final model. The magenta line is the top of the Nazca slab from the Slab2 model (Hayes *et al.* 2018) as a point of reference.

Figure S8. All depth slices through our synthetic checkerboard test. The black solid contours denote the location of + 5 per cent and the dashed contours −5 per cent *Vp* of our synthetic input, respectively. Each checker box is 2 × 2 × 2 model nodes in volume. The grey line shows the ≥ 0.2 hit-quality contour which we use as an indication of resolution in our final model. The magenta line is the top of the Nazca slab from the Slab2 model (Hayes *et al.* 2018) as a point of reference.

Figure S9. Depth slices through our synthetic slab test. The black solid contours denote the location of + 5 per cent *Vp* as our synthetic slab input. We note that the synthetic slab extends only to 895 km depth. The grey line shows the ≥ 0.2 hit-quality contour which we use as an indication of resolution in our final model. The magenta line is the top of the Nazca slab from the Slab2 model (Hayes *et al.* 2018) as a point of reference for depths less than 660 km.

Figure S10. Depth slices through a synthetic slab test with a horizontal tear. The black solid contours denote the location of + 5 per cent *Vp* as our synthetic slab input. A horizontal tear was inserted between 60–165 km depth at ∼3°–5° S. The grey line shows the ≥ 0.2 hit-quality contour which we use as an indication of resolution in our final model. The magenta line is the top of the Nazca slab from the Slab2 model (Hayes *et al.* 2018) as a point of reference for depths less than 660 km.

Figure S11. Depth slices through the full *P*-wave velocity model. The depth of each map view is denoted in the bottom right corner. The magenta line represents the top of the Nazca slab at each depth slice from Slab2 (Hayes *et al.* 2018). The green line denotes the location of the trench.

Figure S12. Oceanic crustal thickness versus slab age for subduction velocity 5 cm yr^{-1}, initial slab dip 20°, overriding plate velocity 0 cm yr^{-1} and overriding plate lithosphere 120 km (modified from Huangfu *et al.* 2016). Blue circles indicate the modelled threshold values to produce flat versus steep subduction (Huangfu *et al.* 2016). The CR crust on the Nazca slab favours flat subduction for these model parameters which are similar to the CR subducting beneath Ecuador.

Please note: Oxford University Press is not responsible for the content or functionality of any supporting materials supplied by the authors. Any queries (other than missing material) should be directed to the corresponding author for the paper.

REFERENCES

Alvarado, A. *et al.*, 2018. Seismic, volcanic, and geodetic networks in Ecuador: building capacity for monitoring and research, *Seismol. Res. Lett.,* **89**(2A), 432–439.

Ancellin, M.A., Samaniego, P., Vlastélic, I., Nauret, F., Gannoun, A. & Hidalgo, S., 2017. Across-arc versus along-arc S r-Nd-Pb isotope variations in the E cuadorian volcanic arc, *Geochem. Geophys. Geosyst.,* **18**(3), 1163–1188.

Antonijevic, S.K., Wagner, L.S., Beck, S.L., Long, M.D., Zandt, G. & Tavera, H., 2016. Effects of change in slab geometry on the mantle flow and slab fabric in Southern Peru, *J. geophys. Res.: Solid Earth,* **121**(10), 7252–7270.

Antonijevic, S.K., Wagner, L.S., Kumar, A., Beck, S.L., Long, M.D., Zandt, G., Tavera, H. & Condori, C., 2015. The role of ridges in the formation and longevity of flat slabs, *Nature,* **524**(7564), 212–215.

Araujo, S., Valette, B., Potin, B. & Ruiz, M., 2021. A preliminary seismic travel time tomography beneath Ecuador from data of the national network, *J. South Amer. Earth Sci.,* **111,** 103486. doi:10.1016/j.jsames.2021.103486.

Bishop, B.T., Beck, S.L., Zandt, G., Wagner, L., Long, M., Antonijevic, S.K., Kumar, A. & Tavera, H., 2017. Causes and consequences of flat-slab subduction in southern Peru, *Geosphere,* **13**(5), 1392–1407.

Borrero, C.A. & Castillo, H., 2006. Vulcanitas del S-SE de Colombia: retroarco alcalino y su posible relación con una ventana astenosférica, *Bol. Geol.,* **28**(2), 23–34. https://revistas.uis.edu.co/index.php/revistaboletindegeologia/article/view/855.

Ciardelli, C., Assumpção, M., Bozdağ, E. & van der Lee, S., 2022. Adjoint waveform tomography of South America, *J. geophys. Res.: Solid Earth,* **127**(2), e2021JB022575. doi:10.1029/2021JB022575.

Condori, C., França, G.S., Tavera, H.J., Eakin, C.M., Lynner, C., Beck, S.L. & Villegas-Lanza, J.C., 2021. Variable seismic anisotropy across the Peruvian flat-slab subduction zone with implications for

upper plate deformation, *J. South Amer. Earth Sci.,* **106,** 103053. doi:10.1016/j.jsames.2020.103053.

Cortés, M. & Angelier, J., 2005. Current states of stress in the northern Andes as indicated by focal mechanisms of earthquakes, *Tectonophysics,* **403**(1-4), 29–58.

Dahlen, F.A., Hung, S.-H. & Nolet, G., 2000. Frechet kernels for finite-frequency traveltimes: I. Theory, *Geophys. J. Int.,* **141,** 157–174.

de Kool, M., Rawlinson, N. & Sambridge, M., 2006. A practical grid-based method for tracking multiple refraction and reflection phases in three-dimensional heterogeneous media, *Geophys. J. Int.,* **167**(1), 253–270.

Faccenna, C., Oncken, O., Holt, A.F. & Becker, T.W., 2017. Initiation of the Andean orogeny by lower mantle subduction, *Earth planet. Sci. Lett.,* **463,** 189–201.

Gailler, A., Charvis, P. & Flueh, E.R., 2007. Segmentation of the Nazca and South American plates along the Ecuador subduction zone from wide angle seismic profiles, *Earth planet. Sci. Lett.,* **260,** 444–464.

Gao, Y., Yuan, X., Heit, B., Tilmann, F., van Herwaarden, D.P., Thrastarson, S., Fichtner, A. & Schurr, B., 2021. Impact of the Juan Fernandez Ridge on the Pampean flat subduction inferred from full waveform inversion, *Geophys. Res. Lett.,* **48**(21), e2021GL095509. doi:10.1029/2021GL095509.

Gianni, G.M., Navarrete, C. & Spagnotto, S., 2019. Surface and mantle records reveal an ancient slab tear beneath Gondwana, *Sci. Rep.,* **9**(1), 19774. doi:10.1038/s41598-019-56335-9.

Graindorge, D., Calahorrano, A., Charvis, P., Collot, J.Y. & Bethoux, N., 2004. Deep structures of the Ecuador convergent margin and the Carnegie Ridge, possible consequence on great earthquakes recurrence interval, *Geophys. Res. Lett.,* **31**(4). doi:10.1029/2003GL018803.

Guillier, B., Chatelain, J.L., Jaillard, E., Yepes, H., Poupinet, G. & Fels, J.F., 2001. Seismological evidence on the geometry of the orogenic system in central-northern Ecuador (South America), *Geophys. Res. Lett.,* **28**(19), 3749–3752.

Gutscher, M.A., Malavieille, J., Lallemand, S. & Collot, J.Y., 1999. Tectonic segmentation of the North Andean margin: impact of the Carnegie Ridge collision, *Earth planet. Sci. Lett.,* **168**(3-4), 255–270.

Gutscher, M.A., Spakman, W., Bijwaard, H. & Engdahl, E.R., 2000. Geodynamics of flat subduction: seismicity and tomographic constraints from the Andean margin, *Tectonics,* **19**(5), 814–833.

Hardy, N.C., 1991. Tectonic evolution of the easternmost Panama Basin: some new data and inferences, *J. South Amer. Earth Sci.,* **4**(3), 261–269.

Hayes, G.P., Moore, G.L., Portner, D.E., Hearne, M., Flamme, H., Furtney, M. & Smoczyk, G.M., 2018. Slab2, a comprehensive subduction zone geometry model, *Science (80-.),* **362**(6410), 58–61.

Hidalgo, S., Gerbe, M.C., Martin, H., Samaniego, P. & Bourdon, E., 2012. Role of crustal and slab components in the Northern Volcanic Zone of the Andes (Ecuador) constrained by Sr–Nd–O isotopes, *Lithos,* **132,** 180–192.

Hu, J. & Liu, L., 2016. Abnormal seismological and magmatic processes controlled by the tearing South American flat slabs, *Earth planet. Sci. Lett.,* **450,** 40–51.

Huangfu, P., Wang, Y., Cawood, P.A., Li, Z.H., Fan, W. & Gerya, T.V., 2016. Thermo-mechanical controls of flat subduction: insights from numerical modeling, *Gondwana Res.,* **40,** 170–183.

Idárraga-García, J., Kendall, J.-M. & Vargas, C.A.., 2016 Shear wave anisotropy in northwestern South America and its link to the Caribbean and Nazca subduction geodynamics, *Geochem. Geophys. Geosyst.,* **17**(9), 3655–3673.

Kay, S.M., Godoy, E. & Kurtz, A., 2005. Episodic arc migration, crustal thickening, subduction erosion, and magmatism in the south-central Andes, *Bull. geol. Soc. Am.,* **117**(1-2), 67–88.

Kennett, B.L.N. & Engdahl, E.R., 1991. Traveltimes for global earthquake location and phase identification, *Geophys. J. Int.,* **105**(2), 429–465.

Király, Á. *et al.*, 2020. The effect of slab gaps on subduction dynamics and mantle upwelling, *Tectonophysics,* **785,** 228458. doi:10.1016/j.tecto.2020.228458.

Koch, C.D. *et al.*, 2021. Crustal thickness and magma storage beneath the Ecuadorian arc, *J. South Amer. Earth Sci.,* **110,** 103331. doi:10.1016/j.jsames.2021.103331.

Li, C., van der Hilst, R.D., Engdahl, E.R. & Burdick, S., 2008. A new global model for P wave speed variations in Earth's mantle, *Geochem. Geophys. Geosyst.,* **9,** Q05018. doi:10.1029/2007GC001806.

Liu, M. & Gao, H., 2022. Three-dimensional variation of the slab geometry within the South American subduction system, *Geophys. Res. Lett.,* **49**(2), e2021GL095924. doi:10.1029/2021GL095924.

Lonsdale, P., 2005, Creation of the Cocos and Nazca plates by fission of the Farallon plate, *Tectonophysics,* **404**(3-4), 237–264.

Lonsdale, P. & Klitgord, K.D., 1978. Structure and tectonic history of the eastern Panama Basin, *Bull. geol. Soc. Am.,* **89**(7), 981–999.

Lynner, C. *et al.*, 2020. Upper-plate structure in Ecuador coincident with the subduction of the Carnegie Ridge and the southern extent of large mega-thrust earthquakes, *Geophys. J. Int.,* **220**(3), 1965–1977.

Lynner, C., Anderson, M.L., Portner, D.E., Beck, S.L. & Gilbert, H., 2017. Mantle flow through a tear in the Nazca slab inferred from shear wave splitting, *Geophys. Res. Lett.,* **44**(13), 6735–6742.

Manea, V.C., Pérez-Gussinyé, M. & Manea, M., 2012. Chilean flat slab subduction controlled by overriding plate thickness and trench rollback, *Geology,* **40**(1), 35–38.

Meltzer, A. *et al.*, 2019. The 2016 Mw 7.8 Pedernales, Ecuador, earthquake: rapid response deployment, *Seismol. Res. Lett.,* **90**(3), 1346–1354.

Michaud, F., Witt, C. & Royer, J.Y., 2009. Influence of the subduction of the Carnegie volcanic ridge on Ecuadorian geology: reality and fiction, *Geol. Soc. Jpn. Mem.,* **204,** 217–228.

Mohammadzaheri, A., Sigloch, K., Hosseini, K. & Mihalynuk, M.G., 2021. Subducted lithosphere under South America from multifrequency P wave tomography, *J. geophys. Res.: Solid Earth,* **126**(6), e2020JB020704. doi:10.1029/2020JB020704.

Montelli, R., Nolet, G., Masters, G., Dahlen, F.A. & Hung, S.-H., 2004. Global P and PP traveltime tomography: rays versus waves, *Geophys. J. Int.,* **158,** 637–654.

Müller, R.D., Sdrolias, M., Gaina, C. & Roest, W.R., 2008. Age, spreading rates, and spreading asymmetry of the world's ocean crust, *Geochem. Geophys. Geosyst.,* **9**(4), Q04006. doi:10.1029/2007GC001743.

NEIC Earthquake catalogue, 2022. National Earthquake Information Centre, On-line Bulletin, http://earthquake.usgs.gov/earthquakes/search /. (Last accessed 31 December 2022).

Pavlis, G.L. & Vernon, F.L., 2010. Array processing of teleseismic body waves with the USArray, *Comput. Geosci.,* **36**(7), 910–920.

Pesicek, J.D., Engdahl, E.R., Thurber, C.H., DeShon, H.R. & Lange, D., 2012. Mantle subducting slab structure in the region of the 2010 M 8.8 Maule earthquake (30–40 S), Chile, *Geophys. J. Int.,* **191**(1), 317–324.

Portner, D.E. *et al.*, 2020. Detailed structure of the subducted Nazca slab into the lower mantle derived from continent-scale teleseismic P wave tomography, *J. geophys. Res.: Solid Earth,* **125**(5), e2019JB017884. doi:10.1029/2019JB017884.

Portner, D.E., Beck, S., Zandt, G. & Scire, A., 2017. The nature of subslab slow velocity anomalies beneath South America, *Geophys. Res. Lett.,* **44**(10), 4747–4755.

Ranero, C.R., Morgan, J.P., McIntosh, K.D. & Reichert, C., 2003, Bending, faulting, and mantle serpentinization at the Middle America trench, *Nature,* **425,** 367–373.

Rawlinson, N., de Kool, M. & Sambridge, M., 2006. Seismic wavefront tracking in 3D heterogeneous media: applications with multiple data classes, *Explor. Geophys.,* **37**(4), 322.

Regnier, M., Font, Y., Charvis, P., Mercerat, D., Rietbrock, A., Ruiz, M. & Alvarado, A., 2016. Pedernales [Data set]. International Federation of Digital Seismograph Networks. doi:10.7914/SN/XE_2016.

Rodríguez, E.E. *et al.*, 2021. Mantle dynamics of the Andean Subduction Zone from continent-scale teleseismic S-wave tomography, *Geophys. J. Int.,* **224**(3), 1553–1571.

Rosenbaum, G., Sandiford, M., Caulfield, J. & Garrison, J.M., 2019. A trapdoor mechanism for slab tearing and melt generation in the northern Andes, *Geology,* **47**(1), 23–26.

Ruiz, M., 2016. Ecuador RENSIG data, *Data Serv. Newsl.,* **18**(2).https://ds.iris.edu/ds/newsletter/vol18/no2/467/ecuador-rensig-data/

Sallarès, V. & Charvis, P., 2003. Crustal thickness constraints on the geodynamic evolution of the Galapagos Volcanic Province, *Earth planet. Sci. Lett.,* **214**(3-4), 545–559.

Schepers, G., van Hinsbergen, D.J.J., Spakman, W., Kosters, M.E., Boschman, L.M. & McQuarrie, N., 2017. South-American plate advance and forced Andean trench retreat as drivers for transient flat subduction episodes, *Nat. Commun.,* **8**(0316), 15249. doi:10.1038/ncomms15249.

Schmandt, B. & Humphreys, E., 2010. Seismic heterogeneity and small-scale convection in the Southern California upper mantle, *Geochem. Geophys. Geosyst.,* **11**(5), 1–19.

Scire, A., Zandt, G., Beck, S., Long, M., Wagner, L., Minaya, E. & Tavera, H., 2016. Imaging the transition from flat to normal subduction: variations in the structure of the Nazca slab and upper mantle under southern Peru and northwestern Bolivia, *Geophys. J. Int.,* **204**(1), 457–479.

Servicio Geológico Colombiano. 1993. Red Sismologica Nacional de Colombia [Data set]. International Federation of Digital Seismograph Networks. 10.7914/SN/CM.

Seton, M. *et al.*, 2020. A global data set of present-day oceanic crustal age and seafloor spreading parameters, *Geochem. Geophys. Geosyst.,* **21**(10), e2020GC009214.

Siebert, L., Simkin, T. & Kimberly, P., 2011. *Volcanoes of the World*. Berkeley, CA: University of California Press. https://volcano.si.edu/resource_products.cfm#.

Simmons, N.A., Myers, S.C., Johannesson, G. & Matzel, E., 2012. LLNL-G3Dv3: global P wave tomography model for improved regional and teleseismic travel time prediction, *J. geophys. Res.,* **117,** B10302. doi:10.1038/ncomms15249.

Spikings, R.A., Crowhurst, P.V., Winkler, W. & Villagomez, D., 2010. Syn-and post-accretionary cooling history of the Ecuadorian Andes constrained by their in-situ and detrital thermochronometric record, *J. South Amer. Earth Sci.,* **30**(3-4), 121–133.

Sun, M., Bezada, M.J., Cornthwaite, J., Prieto, G.A., Niu, F. & Levander, A., 2022. Overlapping slabs: untangling subduction in NW South America through finite-frequency teleseismic tomography, *Earth planet. Sci. Lett.,* **577,** 117253. doi:10.1016/j.epsl.2021.117253.

Syracuse, E.M. & Abers, G.A., 2006. Global compilation of variations in slab depth beneath arc volcanoes and implications, *Geochem. Geophys. Geosyst.,* **7**(5). doi:10.1029/2005GC001045.

Syracuse, E.M., Maceira, M., Prieto, G.A., Zhang, H. & Ammon, C.J., 2016. Multiple plates subducting beneath Colombia, as illuminated by seismicity and velocity from the joint inversion of seismic and gravity data, *Earth planet. Sci. Lett.,* **444,** 139–149. doi:10.1016/j.epsl.2016.03.050.

Taramón, J.M., Rodríguez-González, J., Negredo, A.M. & Billen, M.I., 2015. Influence of cratonic lithosphere on the formation and evolution of flat slabs: insights from 3-D time-dependent modeling, *Geochem. Geophys. Geosyst.,* **16**(9), 2933–2948.

Trenkamp, R., Kellogg, J.N., Freymueller, J.T. & Mora, H.P., 2002. Wide plate margin deformation, southern Central America and northwestern South America, CASA GPS observations, *J. South Amer. Earth Sci.,* **15**(2), 157–171.

Vaca, S., Vallée, M., Nocquet, J.M. & Alvarado, A., 2019. Active deformation in Ecuador enlightened by a new waveform-based catalog of earthquake focal mechanisms, *J. South Amer. Earth Sci.,* **93,** 449–461. doi:10.1016/j.jsames.2019.05.017.

VanDecar, J.C. & Crosson, R.S., 1990. Determination of teleseismic relative phase arrival times using multi-channel cross-correlation and least squares, *Bull. seism. Soc. Am.,* **80**(1), 150–169.

Van Hunen, J., Van Den Berg, A.P. & Vlaar, N.J., 2002. On the role of subducting oceanic plateaus in the development of shallow flat subduction, *Tectonophysics,* **352**(3-4), 317–333.

Vargas, C.A. & Mann, P., 2013. Tearing and breaking off of subducted slabs as the result of collision of the Panama Arc-Indenter with northwestern South America, *Bull. seism. Soc. Am.,* **103**(3), 2025–2046.

Wada, I. & Wang, K., 2009. Common depth of slab-mantle decoupling: reconciling diversity and uniformity of subduction zones, *Geochem. Geophys. Geosyst.,* **10**(10). doi:10.1029/2009GC002570.

Wagner, L.S., Jaramillo, J.S., Ramírez-Hoyos, L.F., Monsalve, G., Cardona, A. & Becker, T.W., 2017. Transient slab flattening beneath Colombia, *Geophys. Res. Lett.,* **44**(13), 6616–6623.

Yepes, H., Audin, L., Alvarado, A., Beauval, C., Aguilar, J., Font, Y. & Cotton, F., 2016. A new view for the geodynamics of Ecuador: implication in seismogenic source definition and seismic hazard assessment, *Tectonics,* **35**(5), 1249–1279.